

A Mesh-Based Model of Liver Vasculature: Implications for Improved Radiation Dosimetry to Liver Parenchyma for Radiopharmaceuticals

Camilo M. Correa-Alfonso

University of Florida

Julia D. Withrow

University of Florida

Sean J. Domal

University of Florida

Shu Xing

Massachusetts General Hospital

Jungwook Shin

Massachusetts General Hospital

Clemens Grassberger

Massachusetts General Hospital

Harald Paganetti

Massachusetts General Hospital

Wesley E. Bolch (✉ wbolch@ufl.edu)

University of Florida <https://orcid.org/0000-0002-7175-9968>

Original research

Keywords: liver, hepatic vasculature, ICRP computational phantom, radionuclide S-values

Posted Date: January 25th, 2022

DOI: <https://doi.org/10.21203/rs.3.rs-1151866/v1>

License:   This work is licensed under a Creative Commons Attribution 4.0 International License.

[Read Full License](#)

Version of Record: A version of this preprint was published at EJNMMI Physics on April 13th, 2022. See the published version at <https://doi.org/10.1186/s40658-022-00456-0>.

A MESH-BASED MODEL OF LIVER VASCULATURE: IMPLICATIONS FOR IMPROVED RADIATION DOSIMETRY TO LIVER PARENCHYMA FOR RADIOPHARMACEUTICALS

Camilo Correa, MS [ORCID: 0000-0002-9756-6873]

Medical Physics Program, College of Medicine, University of Florida, Gainesville, FL USA 32611

Julia Withrow [ORCID: 0000-0001-6265-3355]

J. Crayton Pruitt Family Dept. of Biomedical Eng., University of Florida, Gainesville, FL USA 32611

Sean Domal, MS [ORCID: 0000-0002-5988-5240]

Medical Physics Program, College of Medicine, University of Florida, Gainesville, FL USA 32611

Shu Xing, PhD [ORCID: 0000-0001-6728-5774]

Massachusetts General Hospital, Harvard Medical School, Boston, MA USA 02115

Jungwook Shin, PhD [ORCID: 0000-0001-9529-1442]

Massachusetts General Hospital, Harvard Medical School, Boston, MA USA 02115

Radiation Epidemiology Branch, National Cancer Institute, Rockville, MD USA 21704

Clemens Grassberger, PhD [ORCID: 0000-0002-4425-4489]

Massachusetts General Hospital, Harvard Medical School, Boston, MA USA 02115

Harald Paganetti, PhD [ORCID: 0000-0002-6257-2413]

Massachusetts General Hospital, Harvard Medical School, Boston, MA USA 02115

Wesley E. Bolch, PhD [ORCID: 0000-0002-7175-9968]

J. Crayton Pruitt Family Dept. of Biomedical Eng., University of Florida, Gainesville, FL USA 32611

FOR REPRINTS AND CORRESPONDENCE CONTACT:

Wesley E. Bolch, PhD, FHPS, FAAPM, FAIMBE

J. Crayton Pruitt Family Department of Biomedical Engineering

University of Florida, Gainesville, Florida 32611-6550

Phone: (352) 273-0303 Email: wbolch@ufl.edu

SHORT TITLE:

A mesh-model of the adult liver vasculature

This work was supported in part by

Grant R01 CA248901 with the National Cancer Institute

Submitted to European Journal of Nuclear Medicine and Molecular Imaging Physics (EJNMMI-Physics)

Abstract

Purpose: To develop a model of the internal vasculature of the adult liver for blood dosimetry in radiation therapy and demonstrate its application to differentiation of radiopharmaceutical decay sites within liver parenchyma separate from those within the organ's blood content. ***Method:*** Computer-generated models of hepatic arterial (HA), hepatic venous (HV), and hepatic portal venous (HPV) vascular trees were created within individual lobe segments of the ICRP adult female and male livers (AFL/AML) via an in-house algorithm based. Hemodynamic and geometric parameters of the main vessels were used as inputs. For each iteration of the algorithm, pressure, blood flow, and vessel radii within each tree were updated as each new vessel was created and connected to the viable bifurcation site. The vascular networks created inside the AFL/AML were then tetrahedralized to coupling to PHITS. Specific Absorbed Fractions (SAF) were computed for monoenergetic alpha particles, electrons, and photons. Dual-region liver models of the AFL/AML were proposed and particle-specific SAF values were computed assuming blood decays as modeled in two regions: (1) sites within explicitly modeled hepatic vessels, and (2) sites within the hepatic blood pool residing outside these vessels to include the liver capillaries and blood sinuses. S-values for 22 radionuclides commonly used in radiopharmaceutical therapy were computed using the dual-region liver models and compared to S-values obtained in a single-region liver model of homogenized liver parenchyma (LP) and liver blood (LB). ***Results:*** Liver models with virtual vasculatures of ~6000 non-intersecting straight cylinders representing the HA, HPV, and HV circulations were created for the ICRP reference AFL and AML. SAF energy profiles were obtained using the single-region and dual-region models. For alpha emitting radionuclides, S-values using the single-region models were approximately 14% and 11% higher than the S-values obtained using the dual-region AFL and AML models, respectively. For beta and auger-electron emitters, S-values based on the single-region model were up to 13% and 11% higher than in the dual-region model for the AFL and AML, respectively. ***Conclusions:*** The methodology employed for the liver can be applied to all major organs of the computational phantom for both improved dosimetry of organ parenchyma.

Keywords: liver, hepatic vasculature, ICRP computational phantom, radionuclide S-values

INTRODUCTION

Organ dose assessment is an integral component of both diagnostic and therapeutic nuclear medicine. Computational methods for organ dosimetry include the MIRD schema (with pre-computed radionuclide S-values), dose-point or voxel kernels, and direct Monte Carlo radiation transport [1]. In each case, a geometric model of the patient is required either in the form a whole-body computational human phantom (reference, patient-dependent, or patient-sculpted) or as a segmented CT image acquired during hybrid imaging (SPECT/CT or PET/CT) [2]. In both approaches, organ anatomy is typically restricted to a model of the organ surface (stylized, NURBS, or polygon mesh) or of the organ volume (collection of image voxels). As such, the organ material composition is assigned as a homogenous mixture of its tissue parenchyma and blood content. X-rays and gamma-rays imaged within a source organ of the patient thus originate from decay sites of the radiopharmaceutical that is either passing through the organ's vascular network or has been taken up by organ parenchyma. However, as the patient's organ dosimetric model is homogeneous in nature, this distinction is generally neglected, and the radiation dose is assigned as its mean value across both tissue constituents. While perhaps well-justified for photons and higher-energy beta particles, this approach will tend to overestimate parenchymal dose for those alpha-particles and lower-energy beta particles emitted from the radiopharmaceutical during organ blood transit.

In this study, we develop a geometrically explicit model of intra-liver blood vasculature and quantify dosimetry improvements through explicit accounting for blood decay sites with focus on the organ's larger vessels where blood self-dose would be prominent for shorter-ranged particles. Due to the complexity of human vasculature and the inherent difficulty associated with reconstructing blood vessels using only medical image datasets, mathematical and numerical models based on functional and physical principles have been proposed. One of the more popular models is that based upon Constrained Constructive Optimization (CCO) [3]. Karch *et al.* generalized the CCO method to develop arterial trees of organ vasculature in three dimensions [4]. In 2018, Crookston *et al.* [5] applied the CCO method in the construction of a hepatic arterial tree for stimulation studies of the infusion and trapping of Y-90 microspheres during hepatic tumor radioembolization. In 2019, Sauer *et al.* similarly created a vascular network in the human liver for use in CT imaging studies of hepatic contrast perfusion [6]. Our work proposes a complete vascular network including the hepatic arterial, portal, and venous blood circulation in the livers of the ICRP reference adult male and adult female human computational phantoms [7], with applications for refined dose assessment of liver parenchyma for internal emitters. The approach used is readily extended to other organs of the body.

MATERIALS AND METHODS

In this study, we have developed a method to generate virtual binary trees of the hepatic arterial, hepatic venous, and hepatic portal venous vasculature within the livers of the adult male and female ICRP reference mesh phantoms. The models are generated by an algorithm based on the main features CCO method [3]. During algorithm execution, geometric and hemodynamic parameters are updated each time a new vessel is created thus ensuring total blood flow is preserved, and that both Poiseuille's law and Murray's law are satisfied at all bifurcation sites.

Description of Vascular Tree Generation

The first stage to create a representative model of human vasculature consists of specifying the organ 3D shape to be perfused and the hemodynamic properties and physical laws from which the trees develop. In the present model, homogenous perfusion of the target volume is achieved through dichotomously branching tree structures. The terminal segments of the tree are required to be uniformly distributed inside the perfused volume and the blood flow at each terminal is assumed to be identical across the whole vascular tree.

In our model, vessels are represented as straight and rigid cylindrical pipes. Each pipe is characterized by geometrical parameters (radius R and length l) and hemodynamics parameters (blood flow Q and pressures at the ends of the pipe P_{in} and P_{out}). Each tree constructed begins from a 'root' segment. This initial segment is created by connecting the 'entry' point from which the tree will be developed to the closest random point from a list of uniformly distributed terminal points (N_{term}) generated inside the volume to be vascularized. The radius of the root segment is computed via Poiseuille's equation as shown in **Equation 1**, assuming a perfusion pressure (P_{perf}) at the entry point, a terminal pressure (P_{term}) at the closest random point, and a terminal blood flow (Q_{term}) in that pipe segment.

$$\Delta P = P_{bif} - P_{term} = Q_{term} \frac{8\mu l}{\pi R^4} \quad (1)$$

Once the root segment is created, the tree is generated by subsequently attaching new terminal segments to the existing tree. An overview of the different stages of the algorithm is demonstrated in **Figure 1**.

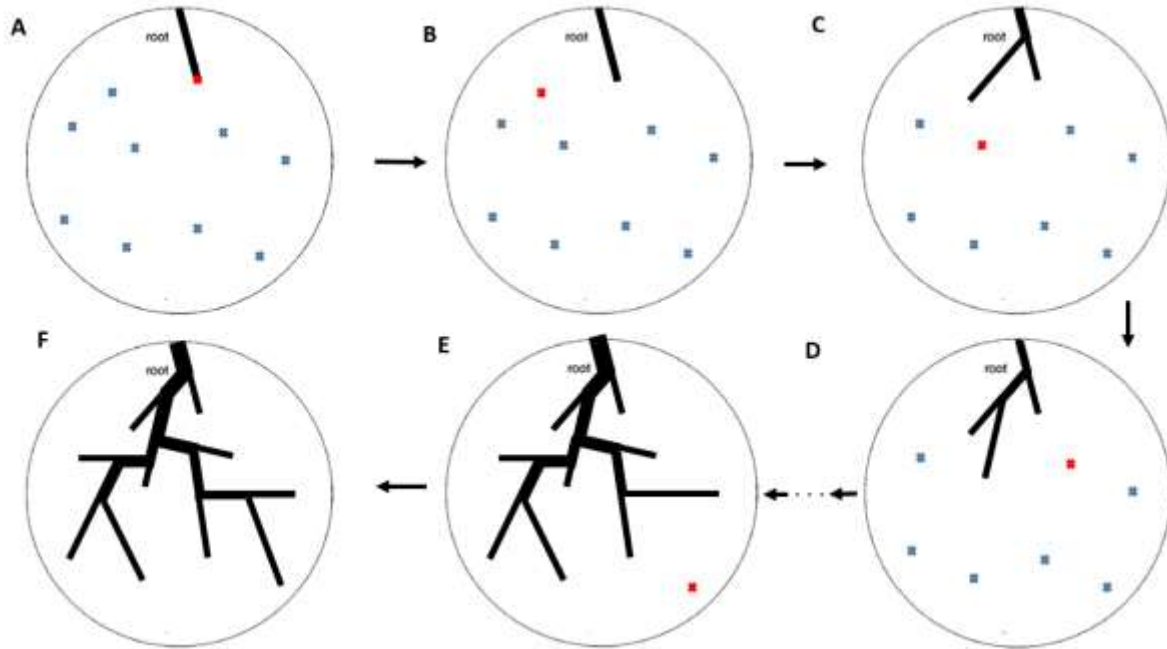


Figure 1. A 2D representation of the in-house vessel generation algorithm developed. **(A)** A single root segment is created. **(B)** The closest point (red cross) from the cloud of terminal random points is selected to be added to the existing tree. **(C)** After the tree is updated, the next closest point to the existing tree is selected. **(D, E)** The vascular tree is grown by connecting a new pipe to the existing tree and updating all hemodynamics and geometrical parameters. **(F)** The final tree is constructed, and the algorithm stops when there are no more terminal points to connect to the tree.

At each iteration, the CCO method chooses the closest random terminal point relative to the center of mass of the existing tree. The mid-point of all segments in the existing tree are evaluated as candidate sites for connection. Later, straight candidate pipes are created from the candidate sites to the chosen terminal point. The same procedure as the one used in the root segment is applied to calculate the radius of each candidate pipe, except the fact that the pressure at the entry of each candidate pipe is equal to the pressure at each candidate site of connections. Finally, the shortest candidate pipe, which is also free of intersections with any other vessel, is chosen and added as a permanent pipe into the tree. Each new permanent pipe added to the existing tree is generated assuming a constant terminal pressure at the pipe end (P_{term}) and a constant terminal blood flow (Q_{term}). The radius of the permanent pipe is computed by using Poiseuille's law [8]. Although blood viscosity μ depends on several factors [9], above a certain diameter, blood could be considered a Newtonian fluid with constant viscosity. Bezy-Wendling and Bruno [8] state that blood is considered a Newtonian fluid for vessels with radii above $50 \mu m$. In our study, the minimum vessel radius is above $100 \mu m$, and thus a constant blood viscosity of $3.5 \text{ mPa}\cdot\text{s}$ is considered.

When connecting a new pipe to the existing tree, two pipes are created: the new pipe and the continuation pipe, as shown in **Figure 2**, with radii R_{new} and R_{con} , respectively. The parent of these two pipes is defined as the 'bifurcation' pipe. Murray's law is next applied to compute the radius R_{bif} of the bifurcation pipe. The 'bifurcation' exponent $\gamma = 3$ was chosen in our study as proposed by Murray [10].

$$R_{bif}^\gamma = R_{new}^\gamma + R_{con}^\gamma \quad (2)$$

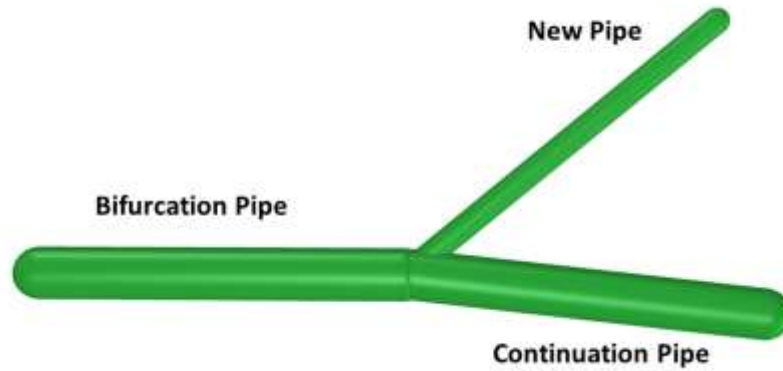


Figure 2. Simplified representation of a bifurcation vessel with two daughters (new and continuation pipes) after the new pipe is permanently added to the virtual tree.

Another physics law considered in the model is the conservation of matter. When a new pipe is connected to the bifurcation site, the blood flow in the bifurcation pipe (Q_{bif}) is conserved as given by **Equation 3**:

$$Q_{bif} = Q_{cont} + Q_{term} \quad (3)$$

From **Equation 3**, Q_{cont} and Q_{term} are the blood flows of the continuation pipe and the new pipe, respectively. The addition of the new pipe produces an increase in the blood volume circulating in the bifurcation pipe with a radius R_{bif} . To account for this increase, the pressure at the entry of the bifurcation pipe needs to be updated. By rearranging **Equation 1**, an expression is obtained for the new pressure at the entry of the bifurcation pipe ($P_{entry-end}$). This new pressure at the bifurcation pipe entry causes that the pressures of all pipes in the path to the root pipe of the tree need to be updated.

$$P_{entry-end} = P_{bif-end} + Q_{bif} \frac{8\mu l_{bif}}{\pi R_{bif}^4} \quad (4)$$

Our model updates all pressures of the pipes each time a new pipe is connected to the tree while maintaining a predetermined pressure (P_{perf}) at the entry point of the root segment.

Main Features of Liver Vasculature

We selected the liver to generate internal vasculature because the liver is a highly vascularized organ that contains at any given time $\sim 10\%$ of the total body blood volume in the adult male and adult female. The liver vascular network, in normal conditions, is very homogenous within the organ volume. Liver human vasculature is unique compared to other human organs as it receives blood from two inlets – the hepatic artery (HA) and hepatic portal vein (HPV) - and drainage occurs via one outlet – the hepatic veins (HV). Oxygenated blood from the HA flows along the HA network and runs analogous to the partially deoxygenated blood from the HPV that circulates through the HPV system. Both inlet systems end at the sinusoids where a mixture of HA and HPV blood occurs. After all metabolic processes take place in the lobules, de-oxygenated blood is extracted from the liver via the HV network, which then passes through the right, middle, or left HV and finally drains into the inferior vena cava.

The anatomy of the liver has been classified using different approaches and patterns [11-14]. In 2000, the Terminology Committee of the International Hepato-Pancreato-Biliary Association presented a universal terminology – the *Brisbane 2000 system* – to avoid confusion and inappropriate use of the terms used to classify the liver [15]. The Brisbane 2000 system adopted the liver segment classification originally proposed by Couinaud [13]. Our work adopts the terminology presented in the Brisbane 2000 system when referring to the segments of the liver.

Another important feature of the liver and its vasculature is that each segment of the liver has its own unique vascular inflow, outflow, and biliary drainage. At each segment, one branch of the HA and one branch of the HPV bring blood to the segment and a branch of the HV drains the blood out of the segment.

In our work, the liver was first divided into segments and branches of the HA, HPV and HV where each segment embodies reference parameters for vessel radius, length, pressure, and blood flow. To create computational vascular models that take into consideration the independent inflow and outflow that occurs in each liver segment, the ICRP adult mesh-type reference computational phantom (MRCP) livers were utilized [7].

Development of Liver Segments and Main Vasculature

Using the Surgical Anatomy of the Liver application from Emory University¹ as an illustrative reference and defining a set of cutting planes and surfaces, the ICRP reference livers were divided into eight segments with similar shapes to those visualized in the application. The percentage of total liver volume (PTLV) for each segment was compared against published experimental data. Mise et al. [16] performed 3D reconstruction and volumetric analysis of 107 normal livers from donor candidates and reported values of PTLV for this cohort. The median values of PTLV reported in this study were used as target parameters in the creation of the segments of AFL/AML. **Table 1** shows the PTLV values from Mise et al. as well as the values obtained after segmentation was performed in the AFL/AML. Relative percentage differences between our values and the reference values for the AFL and AML are less than 1.3% and 0.7%, respectively.

Table 1. PTLV values from a reference study (RS) reported by Mise et al. [16] and from the segmentation performed in the MRCP AFL/AML (present study -PS). PTLV absolute differences between PS and RS are given in the fourth and last columns.

Liver Segments	% of TLV in Male Liver		Absolute Difference	% of TLV in Female Liver		Absolute Difference
	Mise et al.	Present Study		Mise et al.	Present Study	
S1	3.9	3.5	-0.40	4.2	4.0	-0.20
S2	7.9	8.1	0.20	7.6	7.7	0.10
S3	9.8	9.5	-0.30	8.5	8.8	0.30
S4	13.4	13.2	-0.20	13.8	14.0	0.20
S5	12.3	12.1	-0.20	12.7	12.5	-0.20
S6	7.8	7.1	-0.70	8.0	6.7	-1.30
S7	19.9	19.4	-0.50	16.0	17.1	1.10
S8	24.9	24.5	-0.40	26.6	26.5	-0.10

The last step prior the execution of the vessel generation algorithm involves the creation of the main vessels that feed and drain the blood at each liver segment. By using the Emory anatomical model of the liver as a visual guide, and the AFL/AML segments as landmarks, the proper hepatic artery, hepatic portal vein, and a portion of the inferior vena cava including all branches up to the fourth generation were manually constructed using the modeling software Rhinoceros 6.0.² Geometrical parameters including radius and length of each vessel were extracted from Debbaut et al. [17] in which vascular corrosion casting combined with microCT-imaging and image processing were performed to obtain a detailed description of human liver vasculature. Regarding the hemodynamic parameters, a total hepatic blood flow entering the liver of 100 mL/min per 100 g liver wet weight was considered as suggested by Eipel et al. [18].

¹ <http://medapps.emory.edu/surgical-anatomy-of-the-liver/>

² McNeel, R., & others. (2010). Rhinoceros 3D, Version 6.0. Robert McNeel & Associates, Seattle, WA.

According to the anatomical peculiarity of the dual afferent blood supply of the liver, 25% of the total blood entering the liver is oxygenated blood arriving from the proper HA and the other 75% is partially deoxygenated venous blood from the HPV. The pressure value of the proper HA was extracted from Crookston et al [5]. Normal pressures at the HPV and inferior vena cava were obtained from Lebrec et al [19].

Construction of Vascular trees and Solving Intersection of vessel segments

After defining all hemodynamic and geometrical parameters of the constructed main vessels, end pressures and blood flow rates at the main terminal branches that feed and drain each segment were used as inputs for the vessel generation algorithm. With the volume of each liver segment already defined, three terminal branches (from HA, HPV, and HV) of the main vessels were only allowed to end at each liver segment. For each segment, the HA and HPV main terminal branches are used to generate the HA and HPV trees respectively while the HV tree was developed starting at the HV main terminal branch.

The developed vessel generation algorithm was utilized to incorporate HA, HPV, and HV trees at each segment of the MRCP AFL/AML. To define the location of the terminal vessels of the trees, random points were homogeneously generated inside each liver segment. The number of generated random points in each segment was selected in a way that the percentage of the number of points in a segment relative to the total number of points in all segments matched the PTLV values shown in **Table 1**. Using this method, segments with more volume have more terminal points. The total blood flow rate at each liver segment was also assumed to be proportional to the volume of the segment as described by Mise et al [16]. The terminal blood flow rate in each tree developed was assumed to be constant for all terminal segments in the tree.

HA, HPV, and HV trees of all nine liver segments, considering that liver segment IV was divided into components IV-A and IV-B, were generated using the algorithm. At each segment (e.g., Segment VII), the endpoint of the HA, HPV, and HV main vessel branch were made to correspond to the locations where the HA, HPV, and HV trees were developed respectively. At these locations, defined as 'entry points', pressure and blood flow rate are known and defined as P_{perf} and Q_{perf} . In our algorithm, the law of conservation of blood flow rate is considered. Thus, at each liver segment and for each type of tree (HA, HPV, or HV), the total blood flow rate is equal to the summation of the blood flow rates at all terminal vessels. As the terminal blood flow rate is the same for all terminal vessels, Q_{perf} can be represented as:

$$Q_{perf} = \sum_{i=1}^{N_{term}} Q_i = N_{term} * Q_{term} \quad (5)$$

In **Equation 5**, N_{term} is the number of terminal points in a segment, and Q_{term} is the terminal blood flow rate that was defined earlier as constant for all terminal vessels in the tree. In each segment, the same terminal points are used to generate the three types of virtual trees. In this way, HA, HPV, and HV trees are connected at their terminal vessels allowing for closed circulation of blood inside the segment similar to what occurs in real human liver vasculature.

In real vascular trees, one vessel does not intersect with any other vessels in the same network except from the vessel where it emerges, and the vessel branches that originate from itself. During the process of vessel generation in our model, a constraint of non-intersecting vessels was incorporated into the algorithm and referred to as “*Self-Intersection*” restriction. At each iteration of the algorithm in which several candidate new vessel pipes are constructed, the self-intersection restriction was applied to avoid intersection between a selected new pipe and another vessel of the tree at a location different from the bifurcation site. At any iteration, if the shortest candidate new pipe is not free of intersections, the following shortest pipe is checked and the shortest non-self-intersecting pipe is selected as the permanent connection to the tree.

During the development of vascular networks, the volume to perfuse is the same when creating arterial and venous trees. Assuming two different trees are generated in the same volume, one for the arterial and one for the venous circulation, it is important to avoid the creation of venous pipes that could intersect arterial pipes except for the terminal pipes from each tree that end at the same terminal point. Thus, two types of intersections could occur during the generation of a tree when another tree was previously created in the same volume. The intersection of a terminal vessel of a tree with a terminal of vessel of another tree that shares the same terminal point is defined as “*acceptable intersection*”. Acceptable intersections do not need to be avoided as they are needed to create a closed vascular loop. Intersections of vessels of different trees that do not share the same terminal points are defined as “*unacceptable intersections*” and need to be avoided during vessel generation. A function that detects intersections was incorporated inside the algorithm to check if each vessel created overlaps a vessel from another tree. If there is at least one “*unacceptable intersection*” with the new candidate pipe, the new pipe is rejected and the next candidate pipe with the shortest distance to the existing tree is evaluated. Once a new pipe free of unacceptable intersection is found, it is added to the tree as a permanent connection.

To accommodate the blood flow when a new permanent pipe is added to the tree, all radii of bifurcation pipes that are in the path from the new permanent pipe to the root segment increase as defined by Murray’s law. These growths are essential in the algorithm and allow the development of the tree at each iteration. Due to these growths during the tree development, it is possible that one

of the bifurcation pipes in the tree increases in radius sufficiently enough to potentially produce an intersection between the bifurcation pipe and another pipe of a previously constructed tree. Although this event is not frequent, it is more probable to occur in regions with less free space (e.g., near the root segments of each tree). To minimize or eliminate the number of these unacceptable intersections, the other trees generated in the same segment were modified by scaling their pipe's radii by a factor of two. This artificial tree, with twice the original radii of the pipes, was used to check for intersections each time a new vessel was created in the tree under construction. With this solution in place, the number of unacceptable intersections caused by the natural growth of the tree was eliminated or drastically reduced in all trees developed.

At each of the nine segments of the reference liver, HA, HPV, and HV trees were created from the three entry point locations defined by the branches of the main vessels constructed. In total, 27 vascular trees were generated in the AML and AFL independently. About 6000 total blood vessels were created in the vascular networks of both the adult male and adult female liver.

Tetrahedralization of vascular liver models

The minimum vessel radius modeled is approximately 0.1 mm. To incorporate such details in Monte Carlo (MC) radiation transport simulations, tetrahedral mesh-type format was selected [20]. In addition the computation speed using MC transport code PHITS [21] for calculations of dose coefficients in the adult MRCP [22] has been reported to be faster in that mesh geometry than using the original voxelized phantom geometry from ICRP Publication 110 [23].

The AML and AFL with the detailed vascular networks were exported from *Rhinoceros* 6.0 in OBJ format using different organ tag numbers for the vascular models. The tetrahedralization process was performed using the POLY2TET software [24]. The tetrahedral models of vascularized AML and AFL have about 1.4 and 0.9 million tetrahedrons, respectively. Visualization of the tetrahedral AML model with internal virtual vasculature using TETVIEW is shown in **Figure 3**.

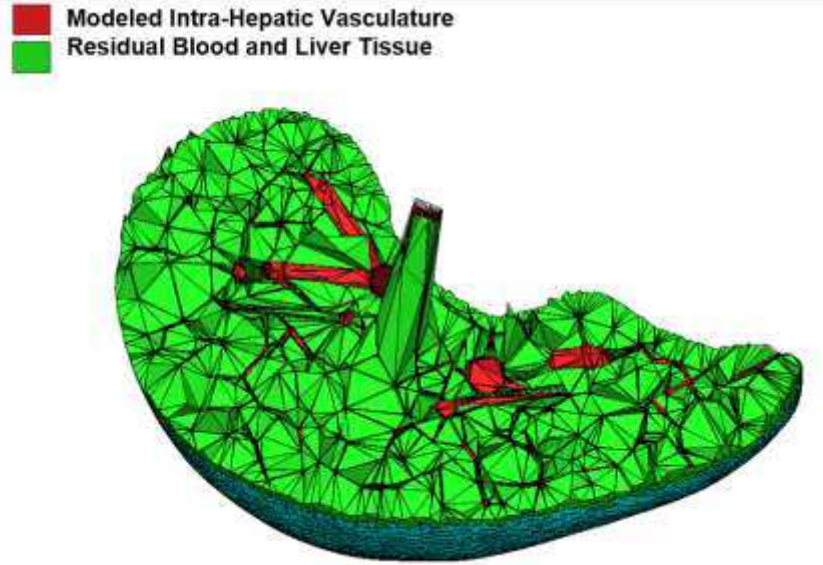


Figure 3. Tetrahedral mesh-type model of the AML. Red Tetrahedrons represent the vascular model generated and green tetrahedrons are a homogenous mixture of residual blood and liver tissue.

Application in radiopharmaceutical therapy: Calculation of radionuclide S-values

Organ dose in radiopharmaceutical dosimetry under the MIRD schema is computed as the product of the time-integrated activity $\tilde{A}(r_S)$, assessed via quantitative imaging, and the radionuclide S-value [25]. Assuming radiation emissions from a source region r_S , the absorbed dose $D(r_T)$ to a target region r_T is calculated as:

$$D(r_T) = \sum_{r_S} \tilde{A}(r_S) S(r_T \leftarrow r_S) \quad (6)$$

where the $\tilde{A}(r_S)$ is typically assessed as the cumulative number of nuclear decays within the source region. $S(r_T \leftarrow r_S)$ is the mean absorbed dose to the target region per nuclei decay in the source region and is computed using the following expression:

$$S(r_T \leftarrow r_S) = \sum_i E_i Y_i \Phi(r_T \leftarrow r_S, E_i) \quad (7)$$

where E_i and Y_i are the energy and yields of the i -th nuclear transformation of the radionuclide, respectively and $\Phi(r_T \leftarrow r_S, E_i)$ is the specific absorbed fraction (SAF) for a radionuclide particle of energy E_i for a given source-target combination. The SAF is defined as the ratio of absorbed fraction (AF - the fraction of the particle energy emitted within the source region that is deposited in the target region) and the target mass:

$$SAF = \Phi(r_T \leftarrow r_S, E_i) = \frac{AF(r_T \leftarrow r_S, E_i)}{m(r_T)} \quad (8)$$

SAF and S values calculations rely on anatomical patient models in which organs are modeled as single region volumes where organ parenchyma and blood are homogeneously combined. Using this single region model for the liver, and considering liver (L) as a homogeneous mixture of liver parenchyma (LP) and liver blood (LB) with mass m_L , for a specific monoenergetic particle, SAF value is calculated as:

$$SAF(L \leftarrow L) = \frac{AF(L \leftarrow L)}{m_L} \quad (9)$$

Under the single region model, $SAF(L \leftarrow L)$ is the approximation used for the ideal case in which LP is both source and target - $SAF(LP \leftarrow LP)$ - and for the case in which LB is the source and LP is the target region - $SAF(LP \leftarrow LB)$. These approximations are due to the lack of an internal vasculature model in which liver blood content is differentiated from the liver parenchyma.

With the liver vascular model presented in this study, it is possible to have more refined approximations for both $SAF(LP \leftarrow LP)$ and $SAF(LP \leftarrow LB)$. Considering this aspect, a dual-region liver model is proposed. The first region is the *liver inside blood vessels* (LIBV) referring to the vascular model created inside the liver. The other one is *liver outside blood vessels* (LOBV) defined as a homogeneous mixture of the residual blood not modeled (any vessel below 0.1mm in radius including capillaries and blood sinuses) and the liver parenchymal tissue. Although the vascular networks created for the AFL/AML do not account for the total blood content in the adult reference livers, having some fraction of the blood model would have an impact on internal dosimetry. We hypothesize that some difference from the single region approximations would be expected for short-range particles that have the chance to deposit their energy completely inside the vascular network. Using the dual-region liver model proposed, $SAF(LP \leftarrow LP)$ can be approximated as:

$$SAF(LP \leftarrow LP) \approx SAF(LOBV \leftarrow LOBV) = \frac{AF(LOBV \leftarrow LOBV)}{m_{LOBV}} \quad (10)$$

Under the assumption of a dual-region liver model, $SAF(LP \leftarrow LB)$ can be obtained as:

$$SAF(LP \leftarrow LB) \approx SAF(LOBV \leftarrow LB) = \frac{f_{BV} \cdot AF(LOBV \leftarrow LIBV) + (1-f_{BV}) \cdot AF(LOBV \leftarrow LOBV)}{m_{LOBV}} \quad (11)$$

where f_{BV} is the fraction of total liver blood mass explicitly modeled within the blood vasculature created.

As previously mentioned, the sinusoids store the mixture of blood from the hepatic arterial and portal circulation. In addition, 60% of blood content in the liver is stored in the sinusoids while the other 40% is blood contained in main vessels, pre-capillaries and capillaries. As our virtual vasculature does not model any vessel below 0.1 mm radius, the vasculature models account for only 13% and 15% of total blood volume content in the AML and AFL, respectively.

MC simulations to compute the AF values were performed with the PHITS transport code v3.24 [21] using the University of Florida HiPerGator computing cluster. Monoenergetic alpha particles, electrons and photons were defined as sources in the single-region liver model and independently in both regions (LIBV and LOBV) of the dual-region liver model. In the single-region liver model, particle sources were randomly sampled within the homogenized mixture of liver blood and liver parenchyma. In the dual-region liver model, two separate simulations were performed in which the particle sources were uniformly distributed in either the LIBV and LOBV regions, respectively. Alpha particle energies ranging from 0.5 MeV to 12 MeV with a step of 0.5 MeV in a linear scale were utilized. For electrons and photons, a logarithmic energy grid from 10 keV to 10 MeV was used. Particle histories were generated giving relative errors in energy deposition tallies below 2% for both single and dual regions. **Table 2** provides details of the MC simulations performed.

All computed S-values were performed using a Python script with SAF interpolation through particle energies using piecewise cubic Hermite interpolation polynomials (PCHIP). S-values were computed for five different radiation classes: (1) photons, (2) beta particles, (3) electrons, (4) alpha particles, and (5) alpha recoil particles. For the last class, the SAF values were interpolated at 2 MeV alpha particle, an approach previously adopted by the ICRP Publication 133 [26].

Table 2. Details of the PHITS transport computations and data post-processing.

Item	Description	Ref.
<i>Code and Version</i>	PHITS v3.24	[21]
<i>Source Description</i>	s-type =24. Particles are produced uniformly from each tetrahedron which belong to the specified universe.	[21]
<i>Cross Sections</i>	PDL97 for photons EGS5 for photons and electrons <i>INCL for nucleons and light ions</i>	[27] [28] [29]
<i>Transport Parameters</i>	Secondary electrons were followed for photon simulations. Alpha particles were simulated down to 0.1 MeV/nucleon, while gammas and electrons were simulated down to 1 keV.	[21]
<i>Variance Reduction</i>	No variance reduction techniques were utilized for this study.	
<i>Statistical Uncertainties and History Numbers</i>	For single-region liver model: 1 million photons, electrons and alpha particles histories were simulated independently at each energy, relative errors in energy deposition tallies were below 2%. For dual-region liver model: 1 million photons, electrons and alpha particles histories were simulated independently at each energy, relative errors in energy deposition tallies were below 2% except for 10 keV electrons and 0.5 MeV alpha particles in which the relative uncertainties were about 3% and 7% respectively.	[21]
<i>Data and Post-Processing</i>	Energy deposited (MeV/source) was tallied in the single region liver model. Absorbed fractions were calculated by normalizing the results to the particle source energy. Energy deposited (MeV/source) was tallied in the LOBV region of the dual-region liver model. Absorbed fractions from the following source- target combinations: (LOBV <- LOBV) and (LOBV <- LIBV) were calculated by normalizing the results to the particle source energy at each target. The fraction of blood mass was used to weight average the absorbed fractions and normalizing by the mass of the target region (LOBV) (See Equation 11).	[21]

RESULTS

Liver vasculature model

Figure 4 shows the final vascular models for AML and AFL. HA, HPV and HV vasculatures are displayed in different colors as shown in the legend. Any self-intersections, unacceptable intersections, and intersections with the outer surface mesh of the liver were eliminated in the final models.

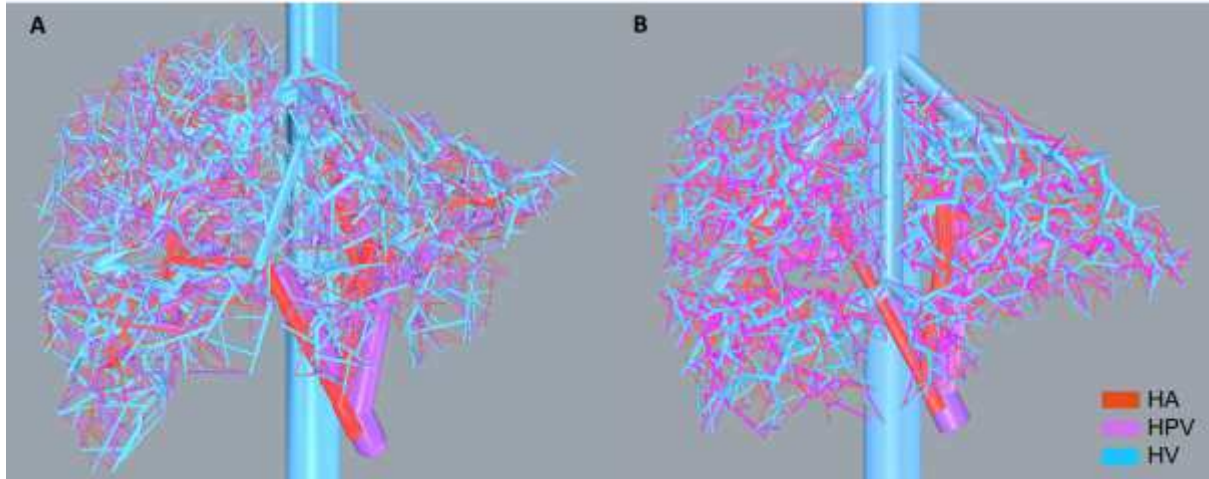


Figure 4. Main vessels and vascular trees generated inside the **(A)** AML and the **(B)** AFL.

To characterize virtual vascular trees and compare them with other models, two parameters are usually referenced: the bifurcation level and the Strahler order. The former is defined as the number of proximal bifurcations from a specific vessel along its path to the root vessel. In the developed models, vessels have been classified depending on the bifurcation level and grouped accordingly. The mean radius of vessels with equal bifurcation level is calculated for each type of vasculature (HA, HPV and HV) in each of our liver models (AML and AFL). The mean radius with its associated standard deviation at each bifurcation level is shown in **Figure 5**. Square and down-triangle symbols were used for the mean radii of the AML and AFL, respectively. Different colors were used to differentiate between the HA, HPV, and HV vascular trees.

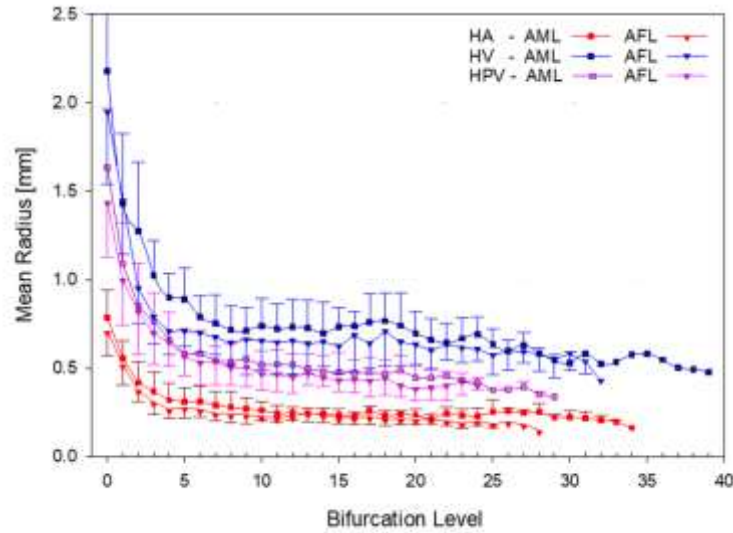


Figure 5. Mean vessel radius per bifurcation level for each type of virtual vasculature created in the AML and AFL. Bars are the standard deviation associated with each mean value.

The Strahler order is utilized to reflect the morphometry of the developed trees. A Strahler order of one was assigned to all terminal vessels. If a bifurcation vessel has two daughter vessels with the same Strahler order, the Strahler order of the daughters plus one is assigned to the bifurcation vessel. If the daughter's vessels have different Strahler orders, the highest of the Strahler order of the daughters will be assigned to the bifurcation vessel. **Figure 6** shows the distribution of vessels per Strahler order for hepatic arterial, hepatic portal and hepatic venous virtual trees in both AML and AFL models.

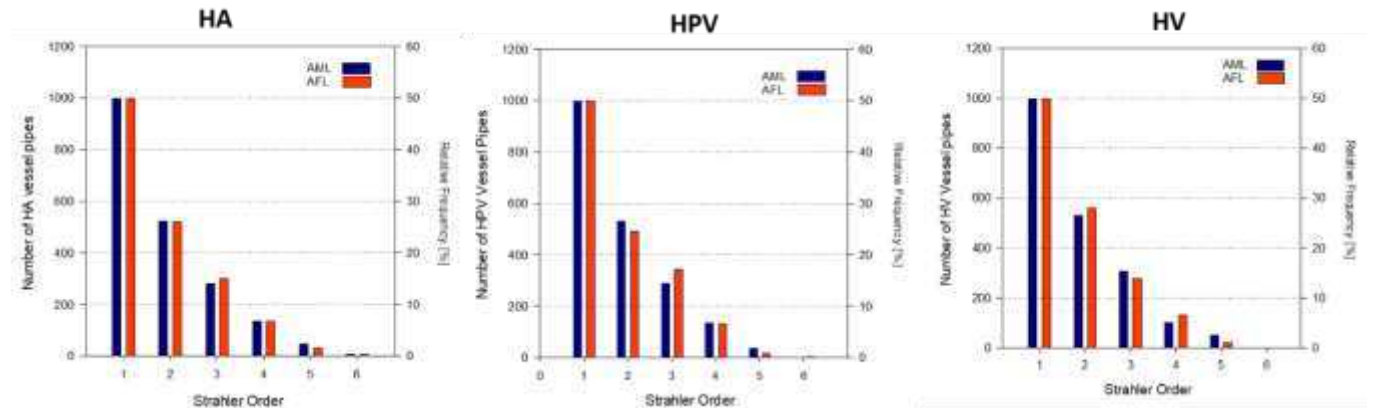


Figure 6. Distribution of virtual vessels of HA, HPV, and HV vascular trees per Strahler Order in AML/AFL.

Liver dosimetry

Specific Absorbed Fractions (SAF) assuming the single-region and the dual-region liver models were calculated using **Equation 9** and **Equations 10** and **11**, respectively. In the proposed dual-region liver model, blood decays were modeled in two stages: (1) sites within explicitly modeled hepatic vessels (LIBV), and (2) residual blood not modeled and liver parenchyma (LOBV).

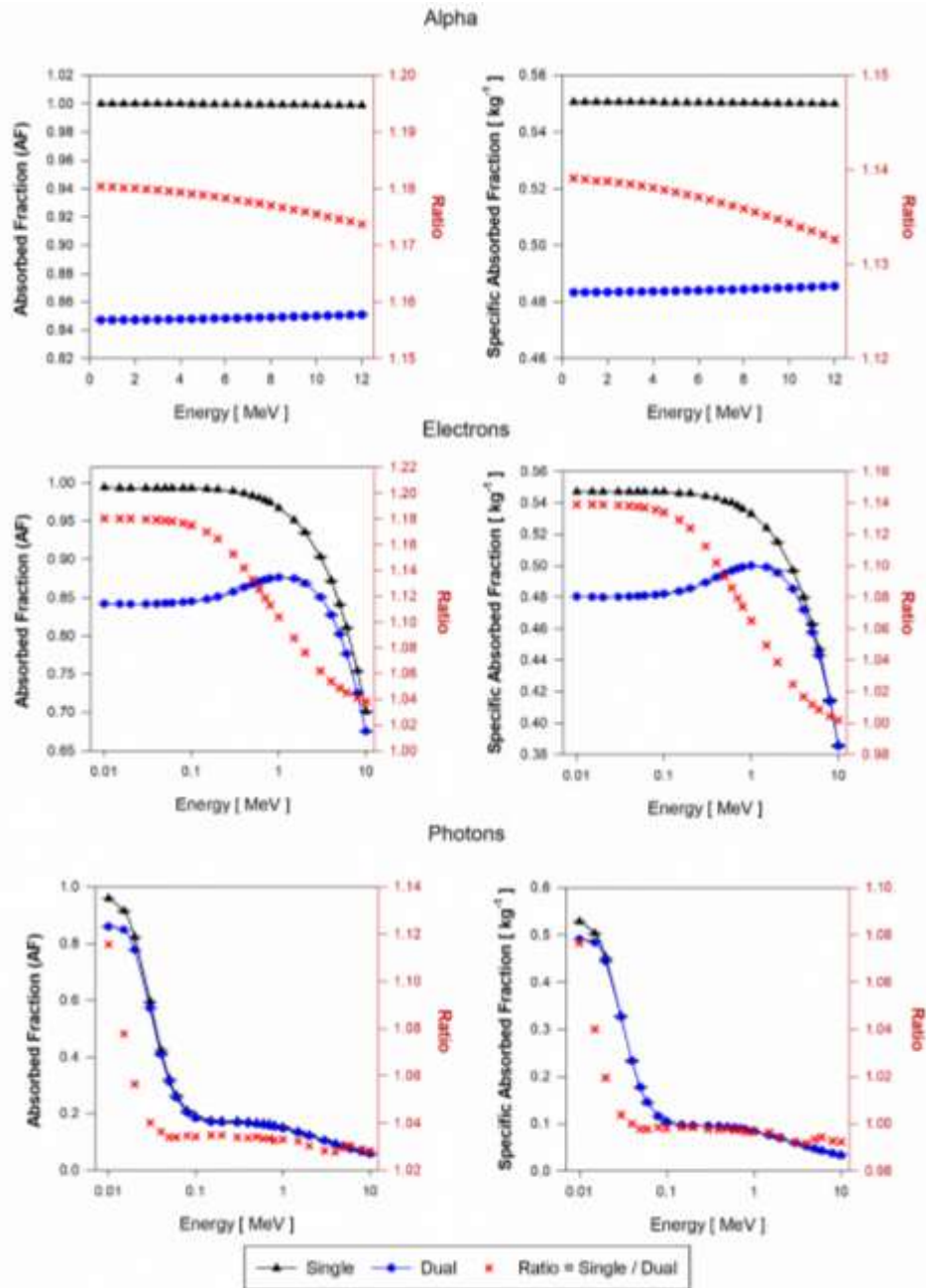


Figure 7. Approximations of $AF(LP \leftarrow LB)$ and $SAF(LP \leftarrow LB)$ for monoenergetic alpha particles (Top), electrons (Center) and photons (Bottom) using the single-region liver model (black triangles) and the dual-region liver model (blue circles) in tetrahedral mesh-type format for the AFL.

Figures 7 and 8 show the AF and SAF values for alpha particles, electrons, and photons sources using both single- and dual-region tetrahedral mesh models of the AFL. Each plot also shows the ratio of the values using the single- and dual-region models. AF and SAF values using the tetrahedral mesh models of the AFL and AML are provided in **Appendices A** and **B**.

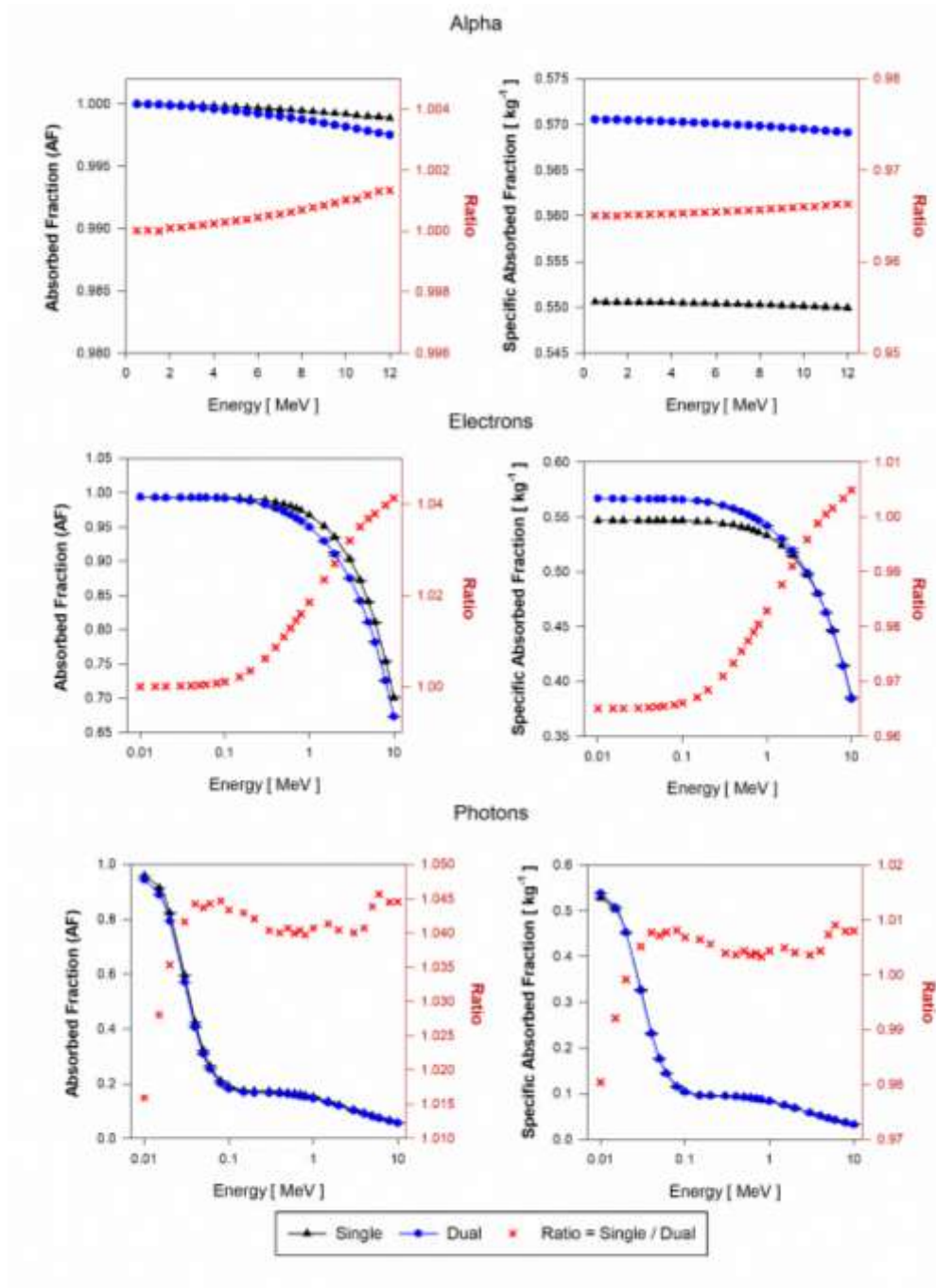


Figure 8. Approximations of $AF(LP \leftarrow LP)$ and $SAF(LP \leftarrow LP)$ for monoenergetic alpha particles (Top), electrons (Center) and photons (Bottom) using the single-region liver model (black triangles) and the dual-region liver model (blue circles) in tetrahedral mesh-type format for the AFL.

DISCUSSION

Morphometric analysis of the vascular models in the AML/AFL

As shown in **Figure 5**, the mean radius decreases as the bifurcation level increases in all types of trees for the AFL and AML models. Mean radii from all trees created in AML are higher than the mean radii of the AFL vascular trees. The difference is caused by a higher total blood flow in the AML compared to that in the AFL model. Due to the high variability of liver vasculature between individuals [30], a morphometric basis comparison of our results with real or modeled human vasculature is difficult to perform. Nevertheless, similar decreasing trends have been reported for the mean radii of virtual and real vascular trees in the liver and other human organs [4, 17, 31].

Figure 6 shows the number of vessels (N) created per Strahler order (SO) for the HA, HPV, and HV trees in both AML and AFL models. The distributions of vessels for the AML and AFL vascular trees are very similar and exhibit exponential decay trends with the increase of the Strahler order. The data in **Figure 6** were fit using an exponential decay function $N = a * e^{-b*SO}$. The coefficients of determination (R^2) were greater than 0.992 in all fits. Similar exponential decay trends have been reported in other computational vascular trees [32, 33].

AF and SAF values from the single- and dual-region models of the AFL/AML

Figure 7 shows the approximations of $AF(LP \leftarrow LB)$ and $SAF(LP \leftarrow LB)$ for the MRCP AFL. For alpha particles, the current methodology using a homogenized liver (single-region liver model) overestimates the AF by about 17.7% across the entire energy range. Following the same analysis but for the SAF values from alpha particles in the AFL, an overestimation of about 14% was found using the single-region model in comparison to our dual-region liver model. It is important to note that the SAF values are obtained as the quotient of the AF values and the target mass. The mass of the single region AFL model (m_L) is 3.5% higher than the target mass (m_{LOBV}) in the dual-region AFL model. This difference reduces the overestimation found in the AF values by 3.5% when analyzing the SAF values obtained from both the single- and dual-region models.

For low energy electrons (less than 100 keV), the AF values calculated using the single region model overestimate by 18% compared to those obtained with the dual-region liver model. Above 100 keV and up to 10 MeV, the ratio of AF using the single-region model and AF using the dual-region model decreases from 1.18 to 1.04. SAF values using the single-region liver model are up to 14% higher than those obtained using the dual-region liver model for electrons below 100 keV. In the dual-region liver model, it is possible the occurrence of events in which the low-energy electrons generated in the LIBV region deposit all the energy in the same region and never reach the LOBV

region. The occurrence of similar events is impossible to discern in the single-region liver model as there is no differentiation between liver tissue and liver blood. At higher electron energies, the probability of these events decreases due to the increase in the electron range compared with the size of the vasculature modeled (LIBV region). Moreover, with the increase of electron energy, the bremsstrahlung radiation increases, and as this electromagnetic radiation is more penetrating, the chances that electrons originating in the LIBV region deposit all their full energy in the same region are also reduced. AF and SAF values for both single- and dual-region models are shown in **Figure 7**.

AF values obtained using the single-region model are up to 12% greater than the AF using the dual-region for very low photon energies (about 10 keV). The ratio of AF values for photons decreases drastically between 10 keV and 40 keV and remain about 1.03 for energies between 50 keV and 10 MeV. The photon SAF values obtained using both models are very similar for all energies except for below 40 keV which yields an SAF ratio increase up to ~ 1.08 .

Figure 8 shows the approximations of $AF(LP \leftarrow LP)$ and $SAF(LP \leftarrow LP)$ for the AFL. For alpha particles, the energy depositions are similar for both models and the AF ratio is about 1.0 for all energies. For alpha SAF values, the single region liver model is 3.5% higher than the SAF calculated using the dual-region. As AF values using both models are almost identical, the SAF ratio is $\sim 3.5\%$, which is explained by the 3.5% excess in the mass of the single-region liver model compared to the LOBV region mass in the dual-region liver model.

For low-energy electrons, AF values using both models are identical and the AF ratio increases up to 1.04 for 10 MeV electrons. Assuming equal AF values for both models, and about 3.5% excess in the mass of the single-region model compared to the dual, SAF values using the single region are underestimated by 3.5%. As electron energy increases above 0.1 MeV, the underestimation of the SAF using the single-region model is compensated by the overestimation (up to 4%) of the single-region model in the AF values calculations.

For low-energy photon sources, the ratio of AF using the single region and the AF using the dual-region model increases from 1.01 to 1.04. Above 30 keV, the single region model overestimates in 4% the AF values. For the photon SAF values above 30 keV, the 3.5% mass excess of the single-region model compared to the dual compensates for the overestimation of about 4% in the AF calculated using the single region.

Approximations of AF and SAF for the two target-source combinations ($LP \leftarrow LB$ and $LP \leftarrow LP$) using the AML single and dual-region models are shown in **Appendix B Figures B.1** and **B.2**, respectively. For all alpha particles and low energy electrons, $AF(L \leftarrow L)$ and $SAF(L \leftarrow L)$ overestimates in 15% and 11.5% respectively compared to those using the dual-region liver model -

$AF(LOBV \leftarrow LB)$ and $SAF(LOBV \leftarrow LB)$. Above 30 keV photons, AF ratios are ~ 1.04 and SAF ratios are ~ 1 . Below 30 keV, ratios of AF and SAF for photons increase up to 1.10 and 1.06, respectively. For the $LP \leftarrow LP$ combination, similar tendencies were found in both single- and dual-region AML models compared to the ones described in **Figure 8** for the adult female liver models.

Computed S-values for alpha, beta, and Auger emitter radionuclides

S-values for 22 radionuclides and 14 additional alpha emitter decay daughters commonly used for internal radiotherapy were successfully calculated using the single- and dual-region liver models. S-values for the AFL and AML models are reported in **Appendix C** and **D**, respectively. From **Table C.1**, it was found that for the approximations of $S(LP \leftarrow LB)$, S-values obtained for the single region liver model are overestimated by up to about 13.7% for several alpha emitters and some of its progeny (At-211, Po-211, Po-212, Po-213, Ra-223, Rn-219, Po-215, Bi-211, Ac-225, Fr-221, At-217, and Th-227). Overestimations of up to 11.4% were found for the same alpha emitters and their progeny using the AML single region model compared to the dual-region model as shown in **Table D.1**.

For all beta emitters included in this study, the S-values calculated using the single region liver model are overestimated. The ratio of S-values defined as the quotient of the single-region S-values - $S(L \leftarrow L)$ - and the dual-region S-value - $S(LOBV \leftarrow LB)$ - ranges from 1.035 for I-124 to 1.117 for Lu-177 for the AFL models and from 1.029 for I-124 to 1.097 for Lu-177 for the AML-MRCP liver models. For Auger electron emitters, S-values using the single-region liver model of the AFL and AML are also overestimated up to 12.9% and 10.8% respectively for Pt-193m. Comparison between $S(L \leftarrow L)$ and $S(LOBV \leftarrow LOBV)$ was also included for all particles in both AML and AFL. Underestimations up to 3.5% for all radionuclides S-values using the single-region models were found.

Limitations and Applications in Blood Dose Assessment in external beam radiotherapy.

The vascular models created in this study for the AFL/AML models have several limitations. First, pre-capillaries, capillaries, and sinuses are not considered. By excluding these structures, the blood volume of our vascular models accounts for only 15% and 13% of the reference blood volume in the AFL and AML, respectively. Although our models do not account for the total blood volume in the livers, main arteries and veins of radius ranging from several millimeters to 0.1 mm are modeled for the arterial, hepatic portal and hepatic venous blood circulations. Another limitation of our model is that it does not include any anastomosis present in real liver vasculature, and rather considers that

each liver segment has just one vessel of each type (HA, HPV, and HV) from which the vascular trees develop.

Beyond applying our models to refine S-value calculations for organ dose assessment in radiopharmaceutical therapy, the vascular models presented in our study have been utilized to develop a 4D dynamic liver blood flow model that allows accurate dose assessment to circulating blood cells during external beam radiotherapy [34]. Using an explicit Monte Carlo simulation that tracks the propagation of blood particles along the liver vascular pathways, blood dose-volume histograms (bDVH) can be generated and the impact of treatment modality, delivery time, and fractionation on circulating blood can be explored.

CONCLUSIONS

A dual-region liver model that differentiates between the main vasculature and the liver parenchyma was developed and SAF values for monoenergetic alpha particles, electrons, and photons were compared to results from the single-region model of the liver from ICRP Publication 133. SAF values computed using the single-region model were overestimated by up to 14% for alpha particles and low-energy electrons. S-values were calculated for several radionuclides used in radiopharmaceutical therapy showing that S-values using the single-region liver models were overestimated by 14%. Our study provides enhanced models to refine the SAF and S-value calculations, essential for a better estimation of organ dose in radiopharmaceutical dosimetry.

Acknowledgements – not applicable

Author Contributions – CC, JW, and SD developed the mathematical algorithm for blood vessel generation, constructed the major vessels in the adult male and adult female liver, applied the CCO algorithm, constructed the tetrahedral model, and performed all PHITS radiation transport simulations. CG, HP, and WB contributed, along with CC, JW, and SD in the study design. SX and JS further contributed to data organization and analysis. All authors contributed to the writing and review of the final manuscript.

Funding – This work was supported by R01 CA248901 (*Developing whole-body computational phantoms for blood dosimetry to model the impact of radiation on the immune system*) by the National Cancer Institute.

Availability of Data and Materials – The polygon mesh and tetrahedral mesh models of the reference adult male and reference adult female liver are available upon request to the Corresponding Author.

DECLARATIONS

Ethics approval and consent to participate – Not applicable.

Consent for publication – Not applicable.

Competing interests – The authors declare that they have no competing interests.

REFERENCES

1. Bartlett, R.M., W.E. Bolch, A.B. Brill, Y.K. Dewaraja, F.H. Fahey, D.R. Fisher, R.F. Hobbs, R.W. Howell, R.F. Meredith, J.G. Rajendran, G. Sgouros, and P. Zanzonico, *MIRD Primer 2020: A Complete Guide to Radiopharmaceutical Dosimetry*. 2021, Reston, VA: The Society of Nuclear Medicine and Molecular Imaging (SNMMI).
2. Bolch, W., C. Lee, M. Wayson, and P. Johnson, *Hybrid computational phantoms for medical dose reconstruction*. *Radiat Environ Biophys*, 2010. **49**(2): p. 155-168.
3. Schreiner, W., *Computer generation of complex arterial tree models*. *J Biomed Eng*, 1993. **15**(2): p. 148-150.
4. Karch, R., F. Neumann, M. Neumann, and W. Schreiner, *A three-dimensional model for arterial tree representation, generated by constrained constructive optimization*. *Comput Biol Med*, 1999. **29**(1): p. 19-38.
5. Crookston, N.R., G.S.K. Fung, and E.C. Frey, *Development of a customizable hepatic arterial tree and particle transport model for use in treatment planning*. *IEEE Trans Radiat Plasma Med Sci*, 2019. **3**(1): p. 31-37.
6. Sauer, T.J., E. Abadi, P. Segars, and E. Samei, *Anatomically and computationally informed hepatic contrast perfusion simulations for use in virtual clinical trials*, in *SPIE Medical Imaging*. 2019: San Diego, CA.
7. ICRP, *ICRP Publication 145: Adult mesh-type reference computational phantoms*. *Ann ICRP*, 2020. **49**(3): p. 1-203.
8. Bezy-Wendling, J. and A. Bruno, *A 3D dynamic model of vascular trees*. *J. Biol. Syst.*, 1999. **7**(1): p. 11-31.
9. Pries, A.R., D. Neuhaus, and P. Gaehtgens, *Blood viscosity in tube flow: dependence on diameter and hematocrit*. *Am J Physiol*, 1992. **263**(6 Pt 2): p. H1770-1778.
10. Murray, C.D., *The physiological principle of minimum work applied to the angle of branching of arteries*. *J Gen Physiol*, 1926. **9**(6): p. 835-841.
11. Hjortsjo, C.H., *The topography of the intrahepatic duct systems*. *Acta Anat (Basel)*, 1951. **11**(4): p. 599-615.
12. Healey, J.E., Jr. and P.C. Schroy, *Anatomy of the biliary ducts within the human liver; analysis of the prevailing pattern of branchings and the major variations of the biliary ducts*. *AMA Arch Surg*, 1953. **66**(5): p. 599-616.
13. Couinaud, C., *Lobes et segments hépatiques: notes sur l'architecture anatomiques et chirurgicale du foie*. *Presse. Med.*, 1954. **62**: p. 709-712.
14. Goldsmith, N.A. and R.T. Woodburne, *The surgical anatomy pertaining to liver resection*. *Surg Gynecol Obstet*, 1957. **105**(3): p. 310-318.
15. Strasberg, S.M., *Nomenclature of hepatic anatomy and resections: a review of the Brisbane 2000 system*. *J Hepatobiliary Pancreat Surg*, 2005. **12**(5): p. 351-355.
16. Mise, Y., S. Satou, J. Shindoh, C. Conrad, T. Aoki, K. Hasegawa, Y. Sugawara, and N. Kokudo, *Three-dimensional volumetry in 107 normal livers reveals clinically relevant inter-segment variation in size*. *HPB (Oxford)*, 2014. **16**(5): p. 439-447.

17. Debbaut, C., D. Monbaliu, C. Casteleyn, P. Cornillie, D. Van Loo, B. Masschaele, J. Pirenne, P. Simoens, L. Van Hoorebeke, and P. Segers, *From vascular corrosion cast to electrical analog model for the study of human liver hemodynamics and perfusion*. IEEE Trans Biomed Eng, 2011. **58**(1): p. 25-35.
18. Eipel, C., K. Abshagen, and B. Vollmar, *Regulation of hepatic blood flow: the hepatic arterial buffer response revisited*. World J Gastroenterol, 2010. **16**(48): p. 6046-6057.
19. Lebrec, D., P. Sogni, and V. Vilgrain, *Evaluation of patients with portal hypertension*. Baillieres Clin. Gastroenterol., 1997. **11**(2): p. 221-241.
20. Yeom, Y.S., J.H. Jeong, M.C. Han, and C.H. Kim, *Tetrahedral-mesh-based computational human phantom for fast Monte Carlo dose calculations*. Phys Med Biol, 2014. **59**(12): p. 3173-3185.
21. Sato, T., Y. Iwamoto, S. Hashimoto, H. Ogawa, T. Furuta, S. Abe, T. Kai, P. Tasi, N. Matsuda, H. Iwase, N. Shigyo, L. Sihver, and K. Nitta, *Features of Particle and Heavy Ion Transport code system (PHITS) version 3.02*. J Nucl Sci Tech, 2018. **55**(6): p. 684-690.
22. Kim CH, Yeom YS, Nquygen TT, Han MC, Choi C, Lee H, Han H, Shin B, Lee JL, Kim HS, Zankl M, Petoussi-Henss N, Bolch WE, Lee C, Chung BS, Qiu R, and E. KF, *New mesh-type phantoms and their dosimetric applications including emergencies*. Ann ICRP, 2018. **47**: p. 45-62.
23. ICRP, *ICRP Publication 110: Adult reference computational phantoms*. Ann ICRP, 2009. **39**(2): p. 1-165.
24. Han, H., Y.S. Yeom, C. Choi, S. Moon, B. Shin, S. Ha, and C.H. Kim, *POLY2TET: a computer program for conversion of computational human phantoms from polygonal mesh to tetrahedral mesh*. J Radiol Prot, 2020. **40**(4): p. 962-979.
25. Bolch, W.E., K.F. Eckerman, G. Sgouros, and S.R. Thomas, *MIRD Pamphlet No. 21: A generalized schema for radiopharmaceutical dosimetry: Standardization of nomenclature*. J Nucl Med, 2009. **50**(3): p. 477-484.
26. ICRP, *ICRP Publication 133: The ICRP computational framework for internal dose assessment for reference adults: specific absorbed fractions*. Ann ICRP, 2016. **45**(2): p. 1-74.
27. Cullen, D., J. Hubbell, and L. Kissel 1997. *EPDL97: The Evaluated Photon Data Library, '97 Version (UCRL-50400, 6, Rev 5)*. Lawrence Livermore National Laboratory, Livermore, CA.
28. Hirayama, H., Y. Namito, A.F. Bielajew, S.J. Wilderman, and W.R. Nelson, *The EGS5 code system. USA and Japan: SLAC National Accelerator Laboratory and High Energy Accelerator Research Organization, SLAC-R-730 and KEK Report 2005-8*. 2005.
29. Boudard, A., J. Cugnon, J.C. David, S. Leray, and D. Mancusi, *New potentialities of the Liege intranuclear cascade model for reactions induced by nucleons and light charged particles*. Phys. Rev. C 2013. **87**: p. 014606.
30. Catalano, O.A., A.H. Singh, R.N. Uppot, P.F. Hahn, C.R. Ferrone, and D.V. Sahani, *Vascular and biliary variants in the liver: implications for liver surgery*. Radiographics, 2008. **28**(2): p. 359-378.
31. Schreiner, W. and P.F. Buxbaum, *Computer-optimization of vascular trees*. IEEE Trans Biomed Eng, 1993. **40**(5): p. 482-491.
32. Ii, S., H. Kitade, S. Ishida, Y. Imai, Y. Watanabe, and S. Wada, *Multiscale modeling of human cerebrovasculature: A hybrid approach using image-based geometry and a mathematical algorithm*. PLoS Comput Biol, 2020. **16**(6): p. e1007943.
33. Schreiner, W., F. Neumann, M. Neumann, A. End, and S.M. Roedler, *Anatomical variability and functional ability of vascular trees modeled by constrained constructive optimization*. J Theor Biol, 1997. **187**(2): p. 147-158.
34. Xing, S., J. Shin, J. Pursley, C. Correa, N. Depauw, S. Domal, J. Withrow, W.E. Bolch, C. Grassberger, and H. Paganetti, *A dynamic blood flow model to compute absorbed dose to circulating blood cells and lymphocytes in liver external beam radiotherapy*. Phys Med Biol, submitted.

Appendix A

Absorbed fractions (AF) and SAF values for monoenergetic alpha particles, electrons and photons using the single-region and dual-region models of the AFL.

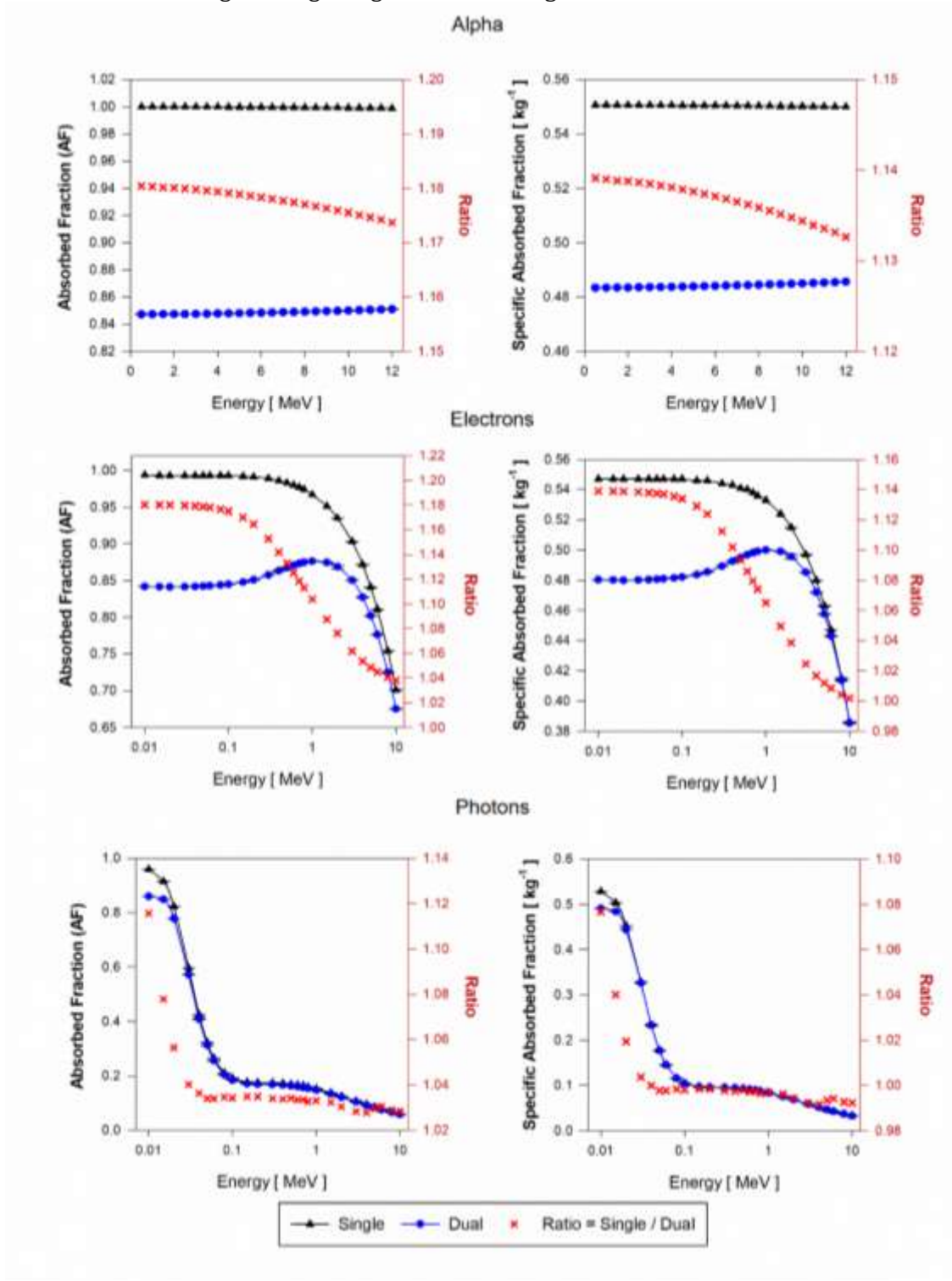


Figure A.1. Approximations of $AF(LP \leftarrow LB)$ and $SAF(LP \leftarrow LB)$ for monoenergetic alpha particles (Top), electrons (Center) and photons (Bottom) using the single-region liver model (black triangles) and the dual-region liver model (blue circles) in tetrahedral mesh-type format for the AFL.

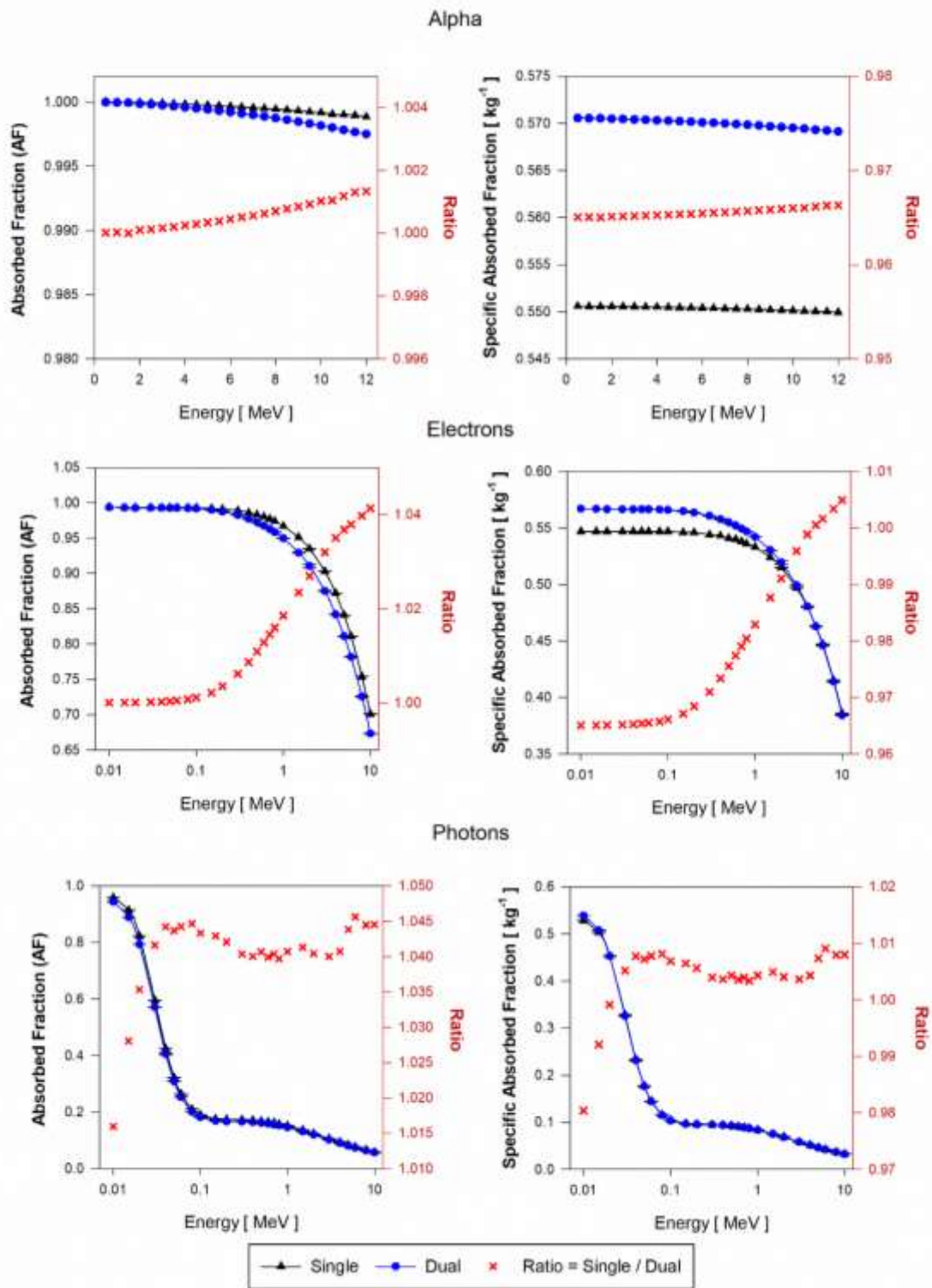


Figure A.2. Approximations of $AF(LP \leftarrow LP)$ and $SAF(LP \leftarrow LP)$ for monoenergetic alpha particles (Top), electrons (Center) and photons (Bottom) using the single-region liver model (black triangles) and the dual-region liver model (blue circles) in tetrahedral mesh-type format for the AFL.

Appendix B

Absorbed fractions (AF) and SAF values for monoenergetic alpha particles, electrons and photons using the single-region and dual-region models of the AML.

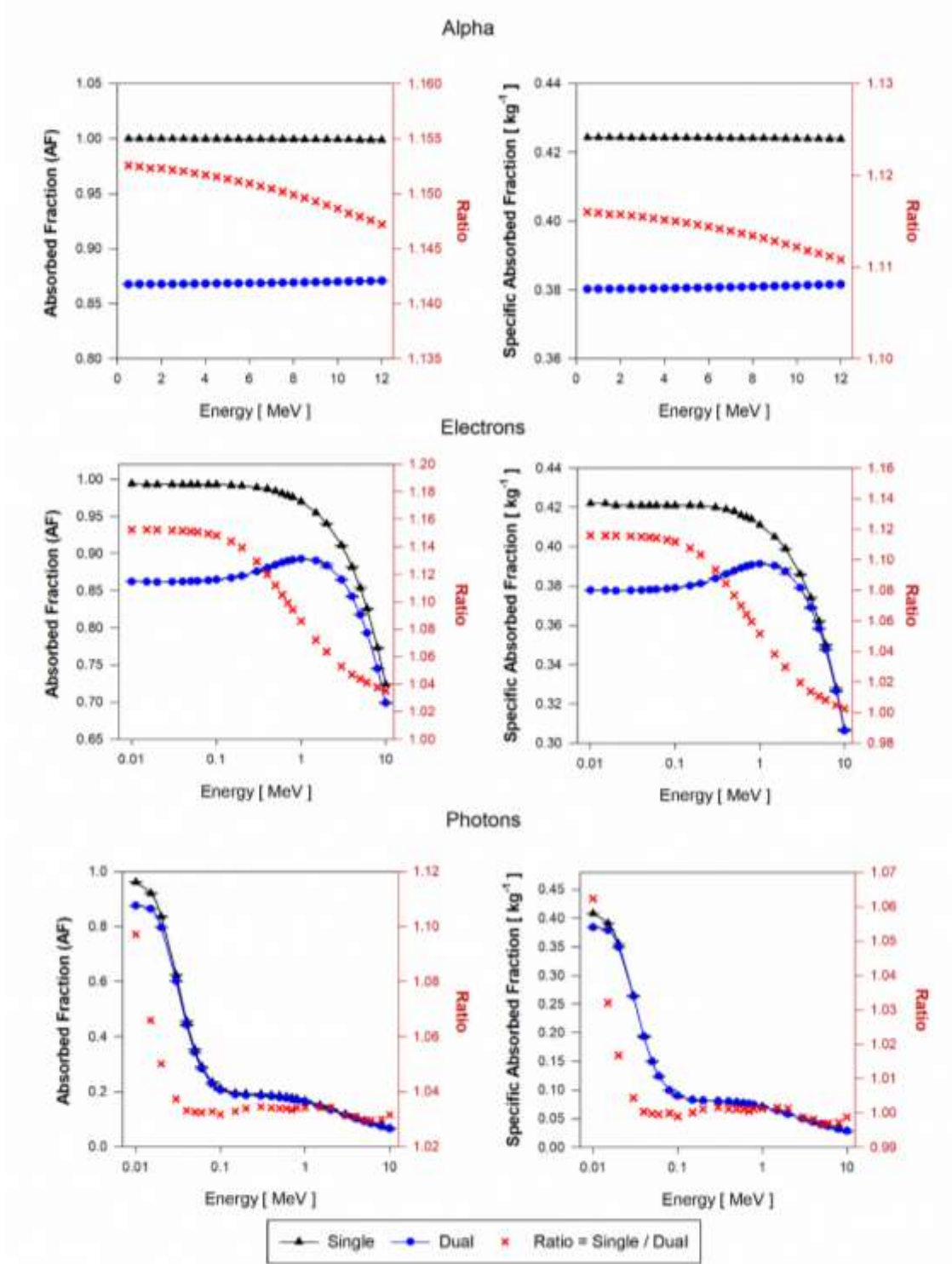


Figure B.1. Approximations of $AF(LP \leftarrow LB)$ and $SAF(LP \leftarrow LB)$ for monoenergetic alpha particles (Top), electrons (Center) and photons (Bottom) using the single-region liver model (black triangles) and the dual-region liver model (blue circles) in tetrahedral mesh-type format for the AML.

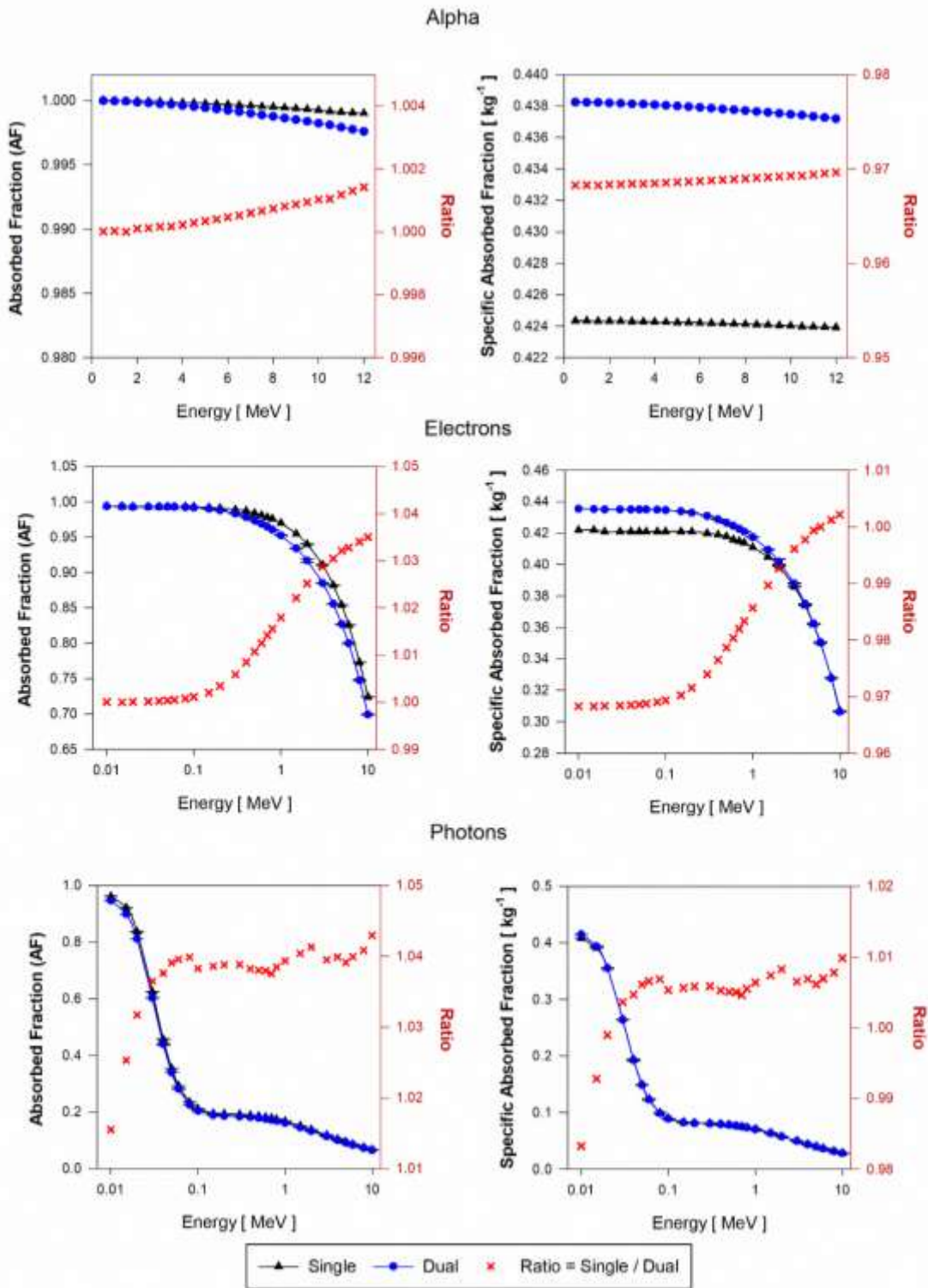


Figure B.2. Approximations of $AF(LP \leftarrow LP)$ and $SAF(LP \leftarrow LP)$ for monoenergetic alpha particles (Top), electrons (Center) and photons (Bottom) using the single-region liver model (black triangles) and the dual-region liver model (blue circles) in tetrahedral mesh-type format for the AML.

Appendix C

S- values for radionuclides using SAF from the single- and dual-region models of the AFL.

Table C.1. Approximations of $S(LP \leftarrow LB)$ and $S(LP \leftarrow LP)$ values for 22 radionuclides (and 14 additional alpha -emitter decay progeny) using the single-region and dual-region tetrahedral mesh models of the AFL

Radionuclide	S-values (mGy/ MBq-s)					
	Approximations to $S(LP \leftarrow LB)$		Ratio	Approximations to $S(LP \leftarrow LP)$		Ratio
	$S(L \leftarrow L)$	$S(LOBV \leftarrow LB)$	$\frac{S(L \leftarrow L)}{S(LOBV \leftarrow LB)}$	$S(L \leftarrow L)$	$S(LOBV \leftarrow LOBV)$	$\frac{S(L \leftarrow L)}{S(LOBV \leftarrow LOBV)}$
<i>Alpha Emitters*</i>						
At-211	2.22E-04	1.95E-04	1.137	2.22E-04	2.30E-04	0.966
(Po-211)	6.69E-04	5.89E-04	1.136	6.69E-04	6.93E-04	0.966
(Bi-207)	3.18E-05	3.11E-05	1.022	3.18E-05	3.19E-05	0.997
Bi-212	2.40E-04	2.14E-04	1.124	2.40E-04	2.48E-04	0.969
(Po-212)	7.90E-04	6.96E-04	1.135	7.90E-04	8.18E-04	0.966
(Tl-208)	8.96E-05	8.60E-05	1.042	8.96E-05	9.05E-05	0.989
Bi-213	5.07E-05	4.64E-05	1.094	5.07E-05	5.20E-05	0.976
(Po-213)	7.53E-04	6.63E-04	1.136	7.53E-04	7.80E-04	0.966
(Tl-209)	8.69E-05	8.26E-05	1.051	8.69E-05	8.77E-05	0.990
(Pb-209)	1.73E-05	1.55E-05	1.114	1.73E-05	1.78E-05	0.971
Ra-223	5.18E-04	4.56E-04	1.136	5.18E-04	5.37E-04	0.966
(Rn-219)	6.08E-04	5.35E-04	1.136	6.08E-04	6.30E-04	0.966
(Po-215)	6.64E-04	5.84E-04	1.136	6.64E-04	6.87E-04	0.966
(Pb-211)	4.02E-05	3.71E-05	1.084	4.02E-05	4.12E-05	0.978
(Bi-211)	5.90E-04	5.19E-04	1.137	5.90E-04	6.11E-04	0.966
(Tl-207)	4.28E-05	3.95E-05	1.084	4.28E-05	4.38E-05	0.978
(Po-211)	6.69E-04	5.89E-04	1.136	6.69E-04	6.93E-04	0.966
Ac-225	5.22E-04	4.59E-04	1.137	5.22E-04	5.41E-04	0.965
(Fr-221)	5.67E-04	4.99E-04	1.137	5.67E-04	5.88E-04	0.966
(At-217)	6.35E-04	5.59E-04	1.137	6.35E-04	6.58E-04	0.966
Th-227	5.37E-04	4.73E-04	1.136	5.37E-04	5.56E-04	0.966
<i>Beta Emitters</i>						
Sr-89	5.03E-05	4.67E-05	1.079	5.03E-05	5.14E-05	0.980
Y-90	7.93E-05	7.46E-05	1.063	7.93E-05	8.04E-05	0.986
I-124	3.24E-05	3.13E-05	1.035	3.24E-05	3.26E-05	0.994
I-131	2.26E-05	2.09E-05	1.083	2.26E-05	2.31E-05	0.979
Sm-153	2.52E-05	2.28E-05	1.107	2.52E-05	2.59E-05	0.973
Ho-166	6.06E-05	5.63E-05	1.076	6.06E-05	6.17E-05	0.982
Lu-177	1.36E-05	1.22E-05	1.117	1.36E-05	1.40E-05	0.970
Re-186	2.97E-05	2.70E-05	1.097	2.97E-05	3.04E-05	0.975
Re-188	6.78E-05	6.34E-05	1.070	6.78E-05	6.89E-05	0.984
<i>Auger e Emitters</i>						
Pd-103	1.54E-06	1.46E-06	1.055	1.54E-06	1.56E-06	0.987
In-111	1.03E-05	9.93E-06	1.035	1.03E-05	1.04E-05	0.993
Sn-117m	1.74E-05	1.58E-05	1.104	1.74E-05	1.79E-05	0.974
I-123	6.16E-06	5.86E-06	1.050	6.16E-06	6.23E-06	0.989
I-125	4.08E-06	3.86E-06	1.057	4.08E-06	4.13E-06	0.987
Pt-193m	1.25E-05	1.11E-05	1.129	1.25E-05	1.30E-05	0.967
Pt-195m	1.82E-05	1.63E-05	1.120	1.82E-05	1.88E-05	0.969

* Radionuclides inside parenthesis for Alpha emitters e.g. (Po-211) correspond to alpha-emitters decay progeny

Appendix D

S- values for radionuclides using SAF from the single- and dual-region models of the AML.

Table D.1. Approximations of $S(LP \leftarrow LB)$ and $S(LP \leftarrow LP)$ values for 22 radionuclides (and 14 additional alpha -emitter decay progeny) using the single-region and dual-region tetrahedral mesh models of the AML

Radionuclide	S-values (mGy/ MBq-s)					
	Approximations to $S(LP \leftarrow LB)$		Ratio	Approximations to $S(LP \leftarrow LP)$		Ratio
	$S(L \leftarrow L)$	$S(LOBV \leftarrow LB)$	$\frac{S(L \leftarrow L)}{S(LOBV \leftarrow LB)}$	$S(L \leftarrow L)$	$S(LOBV \leftarrow LOBV)$	$\frac{S(L \leftarrow L)}{S(LOBV \leftarrow LOBV)}$
<i>Alpha Emitters</i>						
At-211	1.71E-04	1.54E-04	1.114	1.71E-04	1.77E-04	0.969
(Po-211)	5.16E-04	4.63E-04	1.114	5.16E-04	5.32E-04	0.969
(Bi-207)	2.61E-05	2.57E-05	1.019	2.61E-05	2.62E-05	0.999
Bi-212	1.85E-04	1.68E-04	1.103	1.85E-04	1.91E-04	0.972
(Po-212)	6.09E-04	5.47E-04	1.113	6.09E-04	6.28E-04	0.969
(Tl-208)	7.21E-05	6.96E-05	1.035	7.21E-05	7.26E-05	0.993
Bi-213	3.93E-05	3.65E-05	1.078	3.93E-05	4.01E-05	0.979
(Po-213)	5.80E-04	5.21E-04	1.113	5.80E-04	5.99E-04	0.969
(Tl-209)	6.92E-05	6.64E-05	1.042	6.92E-05	6.97E-05	0.993
(Pb-209)	1.33E-05	1.22E-05	1.095	1.33E-05	1.37E-05	0.974
Ra-223	4.00E-04	3.59E-04	1.114	4.00E-04	4.13E-04	0.969
(Rn-219)	4.69E-04	4.21E-04	1.114	4.69E-04	4.84E-04	0.969
(Po-215)	5.11E-04	4.59E-04	1.114	5.11E-04	5.28E-04	0.969
(Pb-211)	3.11E-05	2.91E-05	1.069	3.11E-05	3.17E-05	0.981
(Bi-211)	4.55E-04	4.08E-04	1.114	4.55E-04	4.69E-04	0.969
(Tl-207)	3.31E-05	3.09E-05	1.068	3.31E-05	3.37E-05	0.981
(Po-211)	5.16E-04	4.63E-04	1.114	5.16E-04	5.32E-04	0.969
Ac-225	4.02E-04	3.61E-04	1.114	4.02E-04	4.15E-04	0.969
(Fr-221)	4.37E-04	3.93E-04	1.114	4.37E-04	4.52E-04	0.969
(At-217)	4.89E-04	4.39E-04	1.114	4.89E-04	5.05E-04	0.969
Th-227	4.14E-04	3.72E-04	1.114	4.14E-04	4.27E-04	0.969
<i>Beta Emitters</i>						
Sr-89	3.89E-05	3.65E-05	1.064	3.89E-05	3.95E-05	0.983
Y-90	6.13E-05	5.84E-05	1.051	6.13E-05	6.20E-05	0.989
I-124	2.62E-05	2.55E-05	1.029	2.62E-05	2.63E-05	0.996
I-131	1.79E-05	1.67E-05	1.068	1.79E-05	1.82E-05	0.982
Sm-153	1.95E-05	1.80E-05	1.088	1.95E-05	2.00E-05	0.976
Ho-166	4.68E-05	4.41E-05	1.062	4.68E-05	4.76E-05	0.984
Lu-177	1.05E-05	9.59E-06	1.097	1.05E-05	1.08E-05	0.973
Re-186	2.29E-05	2.12E-05	1.080	2.29E-05	2.34E-05	0.978
Re-188	5.25E-05	4.97E-05	1.057	5.25E-05	5.32E-05	0.987
<i>Auger e Emitters</i>						
Pd-103	1.21E-06	1.15E-06	1.046	1.21E-06	1.22E-06	0.988
In-111	8.44E-06	8.20E-06	1.030	8.44E-06	8.48E-06	0.995
Sn-117m	1.36E-05	1.25E-05	1.086	1.36E-05	1.40E-05	0.977
I-123	4.98E-06	4.79E-06	1.041	4.98E-06	5.03E-06	0.991
I-125	3.22E-06	3.07E-06	1.048	3.22E-06	3.26E-06	0.988
Pt-193m	9.68E-06	8.74E-06	1.108	9.68E-06	9.97E-06	0.970
Pt-195m	1.42E-05	1.29E-05	1.100	1.42E-05	1.46E-05	0.973

* Radionuclides inside parenthesis for Alpha emitters e.g. (Po-211) correspond to alpha-emitters decay progeny